ACS OMEGA

http://pubs.acs.org/journal/acsodf

Article

Comparative Evaluation of Bioefficiency and Photocatalytic Activity of Green Synthesized Bismuth Oxide Nanoparticles Using Three Different Leaf Extracts

Prakash Moorthy and Helen P. Kavitha*

Cite This: *ACS Omega* 2023, 8, 14752−14765

Read Online

ACCESS | Metrics & More | Article Recommendations

ABSTRACT: Nanotechnology has emerged as a promising method for wastewater recycling. In this line, the current study emphasizes the leaf-extract-mediated biosynthesis of bismuth oxide nanostructures (BiONPs) using three different plants, namely *Coldenia procumbens Linn* (Creeping Coldenia), *Citrus limon* (Lemon), and *Murraya koenigii* (Curry) through a greener approach and evaluates their biological properties as well as photocatalytic performance for the first time. As-synthesized BiONPs were physiochemically characterized using UV−visible spectroscopy, Fourier transform infrared (FTIR) spectroscopy, X-ray diffraction (XRD), scanning electron microscopy (SEM), and high-resolution transmission electron microscopy (HRTEM) with energy dispersive X-ray analysis (EDAX). Using the well diffusion method, research on the antibacterial efficiency of BiONPs against human pathogenic Gram-positive bacteria, such as *Staphylococcus aureus* and *Enterococcus faecalis*, and Gram-negative bacteria, including *Escherichia coli* and *Klebsiella pneumonia*, revealed that Gram-negative bacteria exhibited relatively strong activity. The larvicidal activity assessed against *Aedes aegypti* and *Aedes albopictus* mosquito larvae reveals promising larvicidal activity with a minimal dosage of BiONPs with LC_{50} values of 5.53 and 19.24 ppm, respectively, after 24 h of exposure. The excellent photocatalytic activity of as-synthesized BiONPs was demonstrated through the photodegradation of malachite green (MG) and methylene blue (MB) dyes with respective degradation performance parameters of 70 and 90%. The biogenic synthetic approach reported here enables the scalable commercial synthesis of bismuth nanostructures for their widespread use in catalysis for wastewater treatment and environmental cleanup.

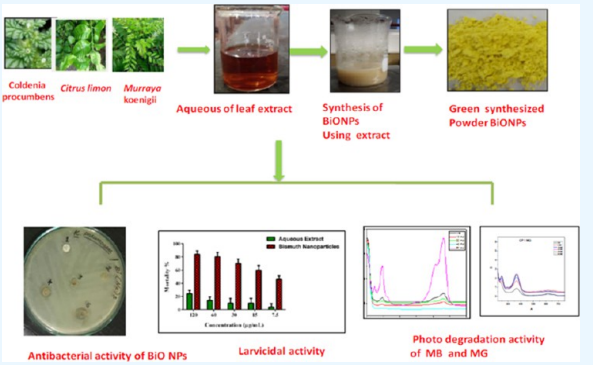

1. INTRODUCTION

Globally, water contamination[1] and its treatment have emerged as a growing concern. In recent decades, remarkable efforts have been made to overcome the challenges of wastewater treatment, as the water pollution level has risen due to an influx of pathogenic microorganisms and toxic pollutants entering the regular water cycle in aquatic environments, which has dire implications for both terrestrial aquatic and ecosystems.[2−6] It is well documented in the literature that wastewater sources are one of the largest conceivable water resources, and their reuse is expected to offset the need for more clean water.[7] In light of these facts, a number of technologies such as sedimentation, coagulation, filtration, adsorption, and membrane technologies have been developed for wastewater treatment; however, they have high operating costs and can introduce dangerous secondary contaminants into the biological system.[8,9]

On the other hand, globally, malaria affects around 350−500 million people annually, resulting in approximately 1 million deaths. Each year, over 2 million malaria cases are reported in India.[10] Lymphatic filariasis, encephalitis, chikungunya, dengue fever, and malaria are transmitted solely by mosquito vectors. *Aedes aegypti* and *Aedes albopictus* were identified as malaria vectors in South India's coastal districts.[11,12] Due to the toxicity and adverse effects of pesticide applications, as well as increased environmental and human health concerns, the use of synthetic chemicals and larvicidal agents is restricted.[13−16] As a result, plant extracts or essential oils may serve as an alternative source of mosquito control agents, as they contain a high concentration of plant-derived compounds that are safe and may be efficient in controlling mosquitoes.[17−19] At the forefront of current nanotechnology research is the development of a dependable green methodology for the ecofriendly

Received: February 7, 2023
Accepted: March 31, 2023
Published: April 17, 2023

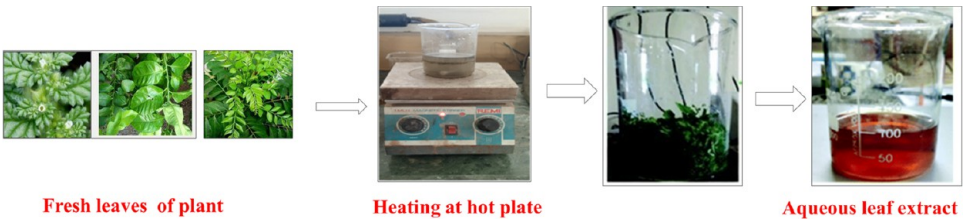

Figure 1. Pictorial representation for the preparation of aqueous leaf extracts.

Table 1. GC-MS Analysis of Identifying the Bioactive Compounds

s. no	leaf used	main bioactive compounds	techniques
1	limon leaves	flavonoids (22.1%), alkaloids (15.87%), saponins (32.87%), and tannins (0.45%)	GC-MS analysis
2	*M. koenigii*	alkaloids: carbazole (18.8%), flavonoids (5.7%), quinones (6.23%), aldehydes (5.89%), terpenoids (11.4%), carotenoids (12.3%), nicotinic acids, phenolics (22.6%), and various vitamins (0.07%)	GC-MS analysis
3	*C. procumbens Linn.*	flavonoids (21.3%), carbohydrates (4.35%), glycosides (1.4%), steroids (0.67%), alkaloids (0.56%), glycosides (3.42%), phytosterols (0.44%), proteins, amino acids (0.87%), fixed oil flavonoids (19.78%), gums, and mucilage.	GC-MS analysis

synthesis of nanoscale compounds using plants as both reducing and capping agents.[20−22] Besides, photocatalyst-assisted environmental remediation has two significant benefits: (i) it transforms contaminants into nonharmful products and (ii) it eliminates the need for extra disposal treatment and toxic chemicals.[23]

The biosynthetic pathway lacks a green strategy despite the abundance of publications examining bismuth-based nanomaterials for varied technologies, including biological, energy, and environment-related applications.[24−26] Bismuth oxide nanostructures are low-cost p-type semiconductors with high X-ray attenuation coefficients, promising photothermal conversion efficiency and microbial activity with a large band gap ranging from 2.0 to 3.96 eV that is essential for effective migration of photoexcited charge carriers. Also, the surface area, surface morphology, crystallographic orientation, and synthesis methodology influence photocatalytic activity. In light of the stated concerns, the plant-extract-mediated biosynthetic method is quite facile, cost-effective, and environmentally benign in relation to conventional hydrothermal and high-temperature chemical syntheses.[27−29]

In view of the above, we developed a facile method to synthesize bismuth oxide nanoparticles using an aqueous leaf extract of *Coldenia procumbens*, *Citrus limon*, and *Murraya koenigii*, and assessed their photocatalytic performance and larvicidal activity. To the best of our knowledge, this is the first attempt to utilize leaf extracts of *C. procumbens*, *C. limon*, and *M. koenigii* for the synthesis of BiONPs. The plant extracts comprise active phytochemicals such as tannins, flavones, aldehydes, saponins, ketones, eugenol, amino acids, terpenoids, and glycosides that are generally water-soluble and offer stability to the nanostructures.[30] Bismuth-based materials are promising due to their photocatalytic, biological, and antibacterial properties. Recently, utilizing bismuth ferrite as a photocatalyst,[31] a new evaluation of performance using the Cat Boost model for MG dye degradation has been reported. The photocatalytic performance of the Bi_2WO_6/ZnO photoanode is shown to remove 100% of COD from municipal wastewater over a period of 180 min.[32] Similarly, Z-scheme CoFe2O4/P-BiOBr heterojunction nanocomposites,[33] sol−gel-derived $BiFeO_3$ nanoparticles,[34] and N-BiOBr/$NiFe_2O_4$ nanocomposites[35] are shown to be promising photocatalysts for environmental remediation applications. Because of their ease of use, abundant biodiversity, and environmental processes, biosynthesis technologies offer great benefits than traditional synthesis techniques.

The synthesized nanoparticles were characterized using FTIR, UV−visible spectrophotometry, X-ray diffraction (XRD), scanning electron microscopy (SEM), transmission electron microscopy (TEM), and energy dispersive X-ray analysis (EDAX). The synthesized BiONPs were tested against pathogenic Gram-positive bacteria, such as *Staphylococcus aureus* and *Enterococcus faecalis*, and Gram-negative bacteria, such as *Escherichia coli* and *Klebsiella pneumonia*. Furthermore, the synthesized BiONPs were tested for larvicidal and photocatalytic activity.

2. MATERIALS AND METHODS

2.1. Chemicals. Bismuth nitrate ($Bi(NO_3)_35H_2O$), ethanol, malachite green, and methylene blue were purchased from Merck. Without additional purification, all of the reagents were employed.

2.2. Plants. Fresh leaves of plants *C. procumbens Linn*, *C. limon*, and *M. koenigii* were collected from Mayiladuthurai District, Vettangudi village (11.28 latitude 79.799 longitude), Tamil Nadu, India.

2.3. Extraction of Aqueous Leave Extracts. The leaves were washed several times with distilled water to remove dust particles and then shadow-dried for 4−5 days to eliminate any excess dampness. The dried CP leaves were ground into a powder using a grinder. Each of the leaf extracts', such as *C. procumbens Linn*, *C. limon*, and *M. koenigii* (1 g), fine powder was mixed with 100 mL of distilled water in a 250 mL measuring glass and heated on a hot plate at 60 °C. The extract was stirred at 600 rpm until it turned dark brown, as shown in Figure 1. The aqueous decoction was filtered 41 times with no. 1 Whatman filter paper and kept at 4 °C for future use. The findings of the gas chromatography−mass spectrometry (GC−MS) analysis of the bioextract to identify the bioactive component are presented in Table 1.

2.4. Green Synthesis of BiONPs. In a 250 mL beaker,1 mM $BiNO_3$ and 20 mL of *C. procumbens Linn.*, *C. limon*, and *M. koenigii* leaf extracts designated L−L, C−L, and CP−L, respectively, were mixed with 80 mL of distilled water and kept at room temperature for 12 h. A change in the color of the solution from yellowish-brown to dark brown indicates the

https://doi.org/10.1021/acsomega.3c00792
ACS Omega 2023, 8, 14752−14765

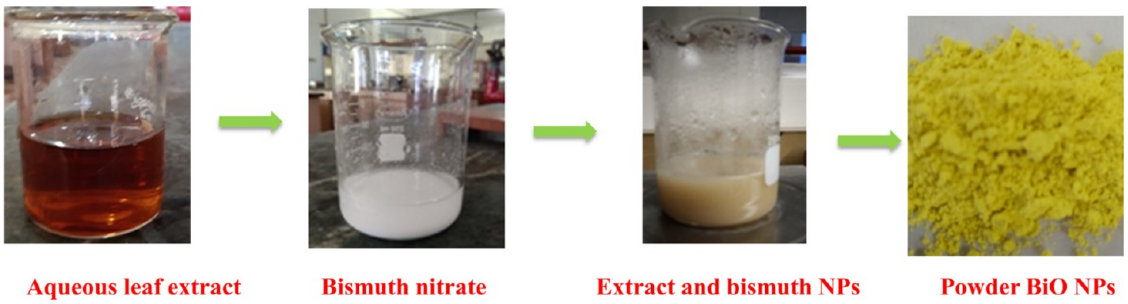

Figure 2. Synthesis of BiONPs using aqueous leaf extracts.

formation of BiONPs. BiONPs were separated by continuous centrifugation at 5000 rpm for 30 min and then dried at 100 °C to obtain a yellow powder, as shown in Figure 2. L-BiONPs, C-BiONPs, and CP-BiONPs, respectively, refer to BiONPs synthesized from L−L, C−L, and CP−L extracts.

2.5. Characterization Techniques. A Shimadzu UV3600 plus spectrophotometer was used to measure UV−visible absorption spectra. An X-ray diffractometer was used to study the crystalline metallic bismuth nanoparticles (PAN Analytical, Netherlands). The KBr pellet method was used to generate Fourier transform infrared (FTIR) spectra. Bismuth nanoparticles were analyzed in the range of 4000−400 cm^{-1} using a Racer 100 Shimadzu FTIR spectrometer. An FEI Squanto 200 SEM instrument was used to examine the morphology of BiONPs using scanning electron microscopy (SEM). Also, the morphology and particle size of BiONPs were determined by TEM (JOELJAPAN, JEM-2100PIUS).

2.6. Evaluation of Antibacterial Activity. The well diffusion method was used to investigate the antibacterial effectiveness against human pathogens, such as *E. coli* and *K. pneumonia* (Gram-negative bacteria) and *S. aureus* and *E. faecalis* (Gram-positive bacteria). On Muller−Hinton agar plates, inoculation bacterial cultures were spread out, followed by the addition of BiONPs and the application of the leaf extract. The drugs were incorporated in a 6 mm well for 24 h, and the agar plates were well incubated at room temperature. The antibiotic used as the positive control was amoxicillin. The zone of inhibition (ZOI) was measured in millimeters (mm) after 24 h of inoculation.

2.7. Assessment of Photocatalytic Activity. Aqueous methylene blue (MB) and methylene green (MG) dyes were used to investigate the photocatalytic activity of BiONPs. The source of illumination was visible light. In 100 mL of an aqueous solution of MB, BiONPs (0.05 g) were distributed (MG). The reaction progress was monitored using UV−visible spectroscopy after the solution combination was exposed to visible light.

2.7.1. Electron Paramagnetic Resonance (EPR). By employing the EPR technique[8] and a Bruker Model EMX X Band electron paramagnetic resonance spectrometer, in situ generations of OH radicals in photocatalytic reactions were investigated (Germany). Utilizing the EPR spectrum, it was determined that hydroxyl radicals can develop in the aqueous phase both in the absence and the presence of catalysts and when exposed to visible light irradiation. Since OH radicals have a short half-life, it is possible to identify the generated species by adding DMPO, a spin-trapping agent. When DMPO was added to the reaction system, the in situ-produced $OH^{\bullet}$ radicals were trapped to form the DMPO-OH adduct, easily detectable by EPR equipment. The right amount of the catalyst, water, and DMPO was added to the reaction tube, which was then exposed to visible light for the allotted time period. Following centrifugation, the sample was poured onto an EPR flat cell, put into the EPR apparatus, and the spectra were recorded.[36]

2.8. Larvicidal Activity of BiONPs. *2.8.1. Insect Rearing.* The larvae of *A. aegypti* and *A. albopictus* were obtained from stagnant water in Chennai and identified at the Kings Institute of Preventive Medicine in Guindy, Chennai. Locally captured early fourth-instar larvae of *A. aegypti* and *A. albopictus* were housed in plastic enamel trays containing dechlorinated tap water. They were kept in the same condition.[37]

2.8.2. Larvicidal Assay. The WHO approach (1996) was used to test the larvicidal activities, with certain modifications, as per (2000). First, 1 mL of an aqueous extract was dissolved in 100 mL of distilled water (stock solution). For the bioassay test of the aqueous extract, 100 ppm of the stock solution was prepared with dechlorinated tap water.[38]

For the bioassay test, five batches of 20 larvae were placed in a breaker, along with 249 mL of dechlorinated water and 1 mL of the specified extract concentration. Dechlorinated tap water was used as the control. After 24 h of exposure, the number of dead larvae was counted, and the mortality percentage was calculated using the average of five replicates. The larval mortality in experimental media was found to be 100%, so it was chosen for the dose−response bioassay. The toxicity test of the BiONPs was performed by placing 20 mosquito larvae into 200 mL of double-distilled H_2O. The BiONPs (100 mg) were dissolved in 1 L of Milli Q water (stock solution). In this study, from the stock solution, different concentrations, such as 25, 20, 15, 10, and 5 ppm, were prepared. Each test had five replicates of each concentration and a control group (distilled water). After 24 h of observation, the acute toxicities on fourth-instar larvae of *A. aegypti* and *A. albopictus* were determined.[39]

2.8.3. Dose−Response Bioassay. Synthesized BiONPs were tested in a dose−response bioassay for larvicidal activity against *A. aegypti* and *A. albopictus* during the laboratory trial. For larvicidal action, different concentrations of synthesized BiONPs were prepared, ranging from 120, 60, 30, 15, and 7.5 ppm. After 24 h of exposure, the number of dead larvae was counted, and the percent mortality was calculated using an average of five repetitions.[40]

2.9. Statistical Analysis. Graph Pad Prism version 6.0 was used to analyze statistical tests (Graph Pad Software, Inc., San Diego). The percentage of larvae and cell viability was represented as mean standard error (SE). After 24 h, the average larvae mortality for nanoformulations was subjected to log probity analysis to determine the LC_{50} and LC_{90}. SPSS software was used to examine the data.

https://doi.org/10.1021/acsomega.3c00792
ACS Omega 2023, 8, 14752−14765

3. RESULTS AND DISCUSSION

The results of UV spectra disclose the optical properties of aqueous leaf extracts as well as synthesized BiONPs, as depicted in Figure 3, which are evaluated by a UV−visible

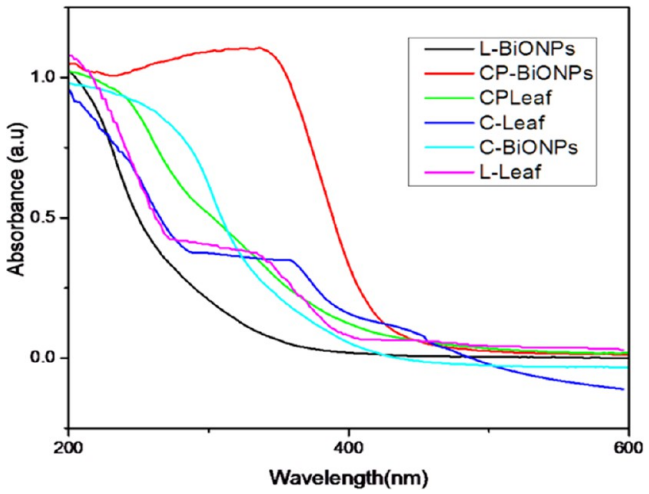

Figure 3. UV−visible spectra of aqueous plant extracts (L−L, C−L, CP−L) and synthesized BiONPs.

spectrophotometer in the range of 250−500 nm. The synthesized BiONthe Ps showed maximum absorbance at 444 nm (CP−L), 418 nm (C−L), and 404 nm (L−L), which confirms the formation of BiONPs. Figure 3 also shows the absorbance spectrum of (L−L, C−L, CP−L) leaf extracts. The absorption edge at 292 nm (CP−L), 274 nm (C−L), and 274 nm (L−L) for the aqueous leaf extract revealed the presence of active phytochemicals in the extract. As inferred from the previous literature, we have confirmed that the aqueous leaf extract possesses phytochemicals like alkaloids, polyphenols, terpenoids, etc.[41] The energy gaps associated with L-BiONPs, C-BiONPs, and CP-BiONPs are determined to be 4.5, 3.6, and 2.8 eV, respectively. We attribute the observed modifications in absorption maxima and energy gap values among the synthesized BiONPs to differences in particle size and the nature of the stabilizers.

XRD analysis is performed to determine the nature of the crystalline phase and the interplanar distance. Figure 4 shows

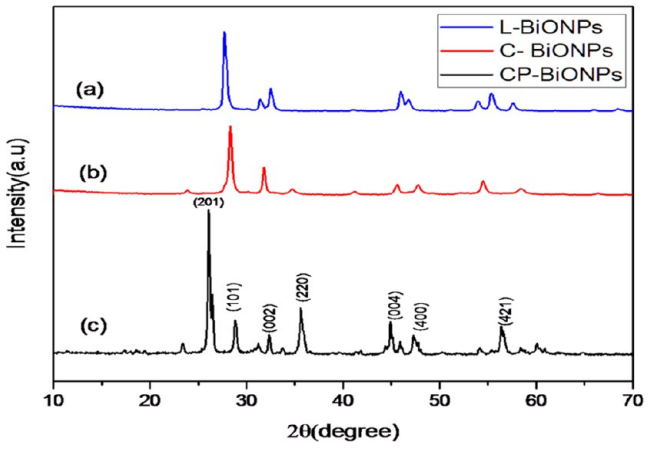

Figure 4. XRD patterns of L-BiONPs (a), C-BiONPs (b), and CP-BiONPs (c).

the XRD patterns of three distinct BiONPs, which display two value peaks at 27.7, 29.2, 31.07, 32.7, 45.76, 45.9, 53.2, 55.47, 57.4, and 73.7°, corresponding to the crystalline planes (201), (101), (002), (220), (004), (400), (131), (421), (402), and (113), respectively, which well matches with the standard JCPDS card no. 27.0050. The appearance of a sharp diffraction peak confirms the good crystalline nature associated with BiONPs. The average crystalline sizes of the BiONPs calculated using the Debye−Scherrer equation $D = k\lambda/\beta \cos\theta$ were found to be 19.55, 19.78, and 20 nm, respectively, for CP-BiONPs, C-BiONPs, and L-BiONPs. The obtained XRD peak confirms the tetragonal phase for the synthesized BiONPs. From Figure 4, it is confirmed that the synthesized BiONPs do not contain any impurities.[42]

FTIR spectra of aqueous leaf extract and synthesized BiONPs are shown in Figure 5. The FTIR analysis confirms

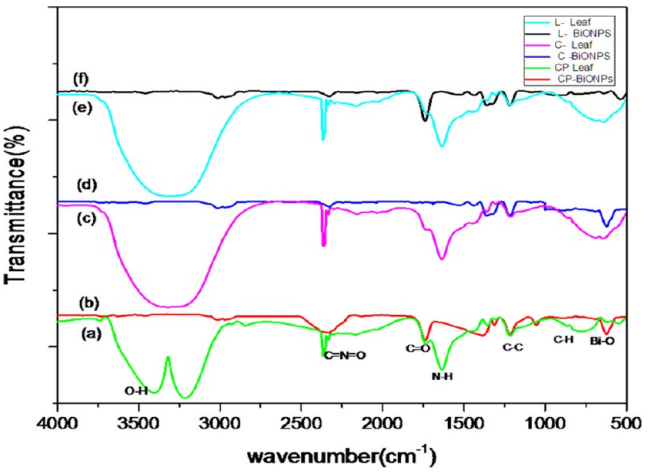

Figure 5. FTIR spectra of synthesized L (f), C (d), CP (b), BiONPs and L−L (e), C−L (c), and CP−L (a), aqueous leaf extracts.

the presence of functional groups in the leaf extract and BiONPs. The peak obtained at 3423 cm^{-1} corresponds to the stretching vibration of O−H present in the aqueous leaf extracts. The hydroxyl group in the aqueous leaf extract plays a vital role in reducing BiONPs and has a strong ability to interact with BiONPs. The peak at 2358 cm^{-1} is due to the NH stretching vibration associated with the aqueous leaf extract. Also, the peak observed at 2329 cm^{-1} is due to the C═N═O asymmetric vibration. The band at 1636 cm^{-1} is due to the stretching vibration of the C═O bond. The spectrum aqueous extract of C−L comprises C−C stretching vibrations at 1432 cm^{-1} and C−H vibrations at 867 cm^{-1}. From the spectrum of L−L, it is to be noted that C−O stretching vibrations appeared at 1328 and 1039 cm^{-1} and C−H vibrations at 814 cm^{-1}. These peaks associated with the plant extract either disappear or are modified in the IR position, which might be involved in reducing bismuth ions. From the results, it could be inferred that the aqueous leaf extract encompasses secondary metabolites that act like capping and stabilizing agents and promote the chemical reduction of a bismuth precursor to form BiONPs.

All three different BiONPs under study exhibit a broad set of peaks between 400 and 750, cm^{-1}, which is attributable to the stretching vibration of the Bi−O−Bi bond. Bi−O metal oxide stretching emerged at 614, 625.41, and 568.01 cm^{-1}, respectively, for CP-BiONPs, C-BiONPs, and L-BiONPs.

https://doi.org/10.1021/acsomega.3c00792
ACS Omega 2023, 8, 14752−14765

The spectral evidence reveals that aqueous leaf extracts that act as a reduction and capping can reduce the bismuth salt into BiONPs. Many researchers have reported that the phytochemicals present in the extract are used as the capping agents, and our results also agree with these studies.[43]

The FESEM micrograph images of the synthesized L-BiONPs, C-BiONPs, and CP-BiONPs are shown in Figure 6.

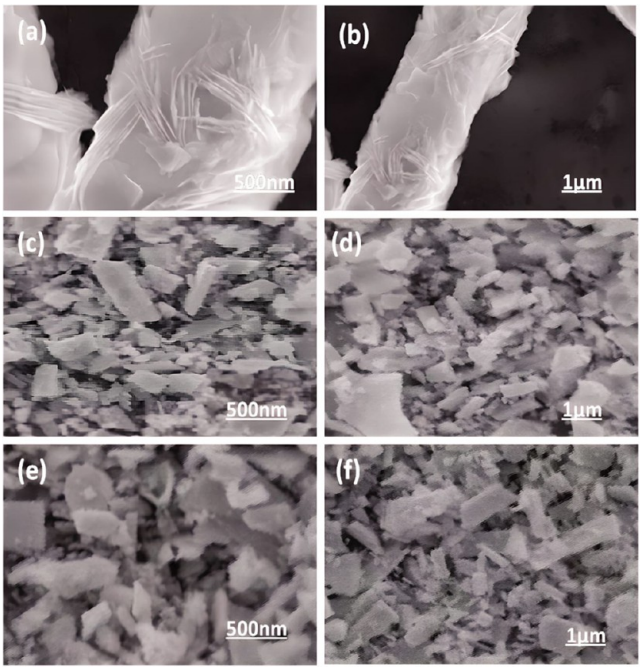

Figure 6. FESEM micrograph of the synthesized (a, b) L-BiONPs, (c, d) C-BiONPs, and (e, f) CP-BiONPs.

The FESEM images clearly show that the synthesized BiONPs are irregularly distributed with rod-like, pear-shaped morphology comprising a number of microscopic holes scattered over the surface. As notable from the images, L-BiONPs, C-BiONPs, and CP-BiONPs exhibit rod-shaped, pear-shaped, and rock-shaped nanostructures, respectively. Therefore, we presume that the surface morphology, particle shape, and size are highly dependent upon the nature of the leaf extract used as a reducing agent, as evident from the results. The presence of nonuniformly dispersed holes over the particle surface of all three kinds of BiONPs might have been created during the biogenic reduction process, owing to the presence of phytochemicals that act both as a capping agent and a stabilizer. We presume that the presence of a fibrous layer formed around the BiONPs is due to the presence of phytochemicals surrounding them. The presence of agglomerated bismuth nanoparticles, as evident from FESEM images, is inevitable during green synthesis due to the lack of control in the phytochemical composition of the bioextract. However, the degree of agglomeration greatly depends upon the nature of the bioextract. Our results agree with earlier studies.[44]

The development of varied shapes, sizes, and nonhomogeneous porous nature associated with BiONPs is attributable to differences in nucleation time and nonuniform distribution of heat zones within the reaction time. This is likely because the bioextract contains surfactants, capping, structure-directing, and protective agents. The BiONPs also display agglomeration, although the borders between single crystallites are visible.

To achieve further insights into the morphology and size of BiONPs, TEM studies were performed, and the results are shown in Figure 7. Upon investigating three different BiONPs, CP-BiONPs revealed better morphology, high product yield, and good crystallinity. Therefore, we conducted TEM and SAED studies for CP-BiONPs.

Before TEM imaging, the BiONP solution was placed on a carbon-coated copper grid and allowed to dry at ambient temperature. The CP-BiONPs were found to be well-segregated, with an approximate particle size of around 20 nm. The crystal size observed in the XRD investigation agrees well with these findings. We infer from the results that the aqueous extract of a CP leaf could be a good and effective material for synthesizing highly stabilized crystalline BiONPs. The SAED pattern also suggests that the BiONPs possess highly ordered crystalline structures. The chemical composition of BiONPs was determined using energy-dispersive X-ray analysis. The identification of prominent peaks of bismuth (Bi), (C), and oxygen (O) elements was confirmed using this technique. From elemental analysis, it is clear that the synthesized BiONPs are free from impurities.

4. ANTIBACTERIAL ACTIVITY STUDIES

The antibacterial efficiency of the synthesized BiONPs of different pathogenic bacteria was investigated using Gram-negative (*E. coli*, *K. pneumonia*) and Gram-positive (*S. aureus* and *E. faecallis*) bacteria through the disc diffusion method. The synthesized CP-BiONPs, C-BiONPs, and L-BiONPs of varied concentrations (5−20 μL) were introduced into plates, and the difference was noted after 24 h of inoculation to evaluate the antibacterial efficiency. The in vitro antibacterial activity of CP-BiONPs, L-BiONPs, and C-BiONPs is shown in Figures 8, 9, and 10, respectively, along with the numerical values tabulated. The results show that both C-BiONPs and L-BiONPs have relatively less activity than CP-BiONPs toward both Gram-positive and Gram-negative strains. It has been proposed that positively charged metal oxides might have interacted with bacteria through electrostatic interaction leading to the inhibition of enzyme production and deactivation of DNA by interacting with negatively charged groups present in the bacterial cell wall, resulting in increased permeability and cell death. The disparity in the effectiveness of different BiONPs against different organisms is subject to the impermeability of the bacterial cell. From the results, it is clear that *K. pneumoniae* (15 mm), a Gram-negative bacterial strain, is effectively inhibited by CP-BiONPs, while against *E. coli* (5 mm) is less. Moderate activity is shown toward *E. faecalis* (8 mm), while growth inhibition against *S. aureus* (1.5 mm) is lower, as evident from Table 2. L-BiONPs exhibited very little activity against *S. aureus* (0 mm) and maximum activity toward *E. coli* (4 mm), which demonstrates that C-BiONPs did not inhibit the development of *K. pneumoniae* (0 mm), but that it did inhibit the growth of *E. coli* (5 mm). According to these findings, CP-BiONPs have an incredible potential for use in the advancement of novel molecules for the deterrent and remedial administration of pathogenic bacterial diseases. The majority of Gram-negative bacteria pathogens might use CP-BiONPs as an antigrowth promoter. It is comprehensible that size, shape, and biosynthesis composition are the three most important aspects that influence microbial activity. The maximum antibacterial activity of CP-BiONPs could be related to the (i) type of surface capping phytochemicals and (ii) tiny particle size, as demonstrated

https://doi.org/10.1021/acsomega.3c00792
ACS Omega 2023, 8, 14752−14765

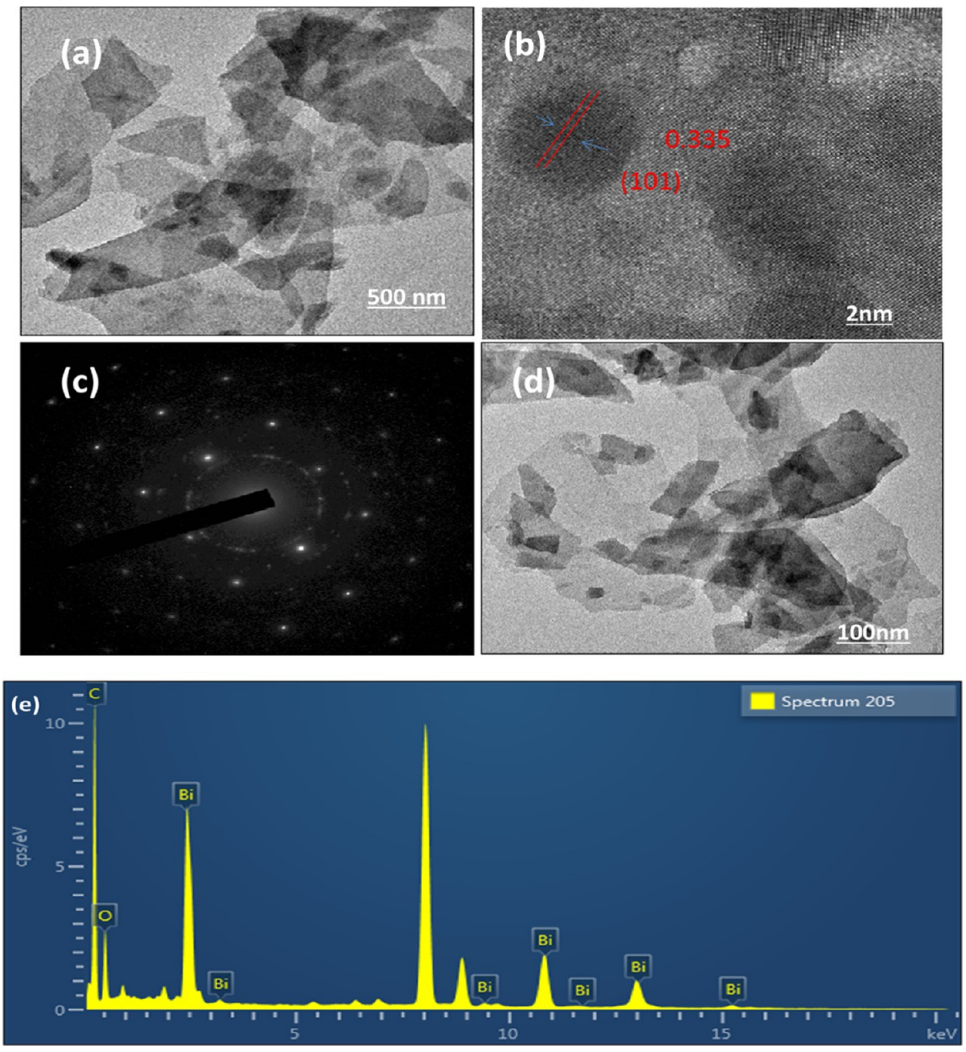

Figure 7. TEM image of the synthesized CP-BiONPs (a, b, d), SAED pattern of CP-BiONPs (c), and EADX analysis of CP-BiONPs (e).

by these results. Subsequently, CP-BiONP species might adhere to its surface, maximizing its reactivity and expanding its harmful impacts against the bacteria.[45−47]

5. LARVICIDAL ACTIVITY STUDIES

The larvicidal efficacy of CP-BiONPs was investigated against fourth-instar larvae of *A. aegypti* and *A. albopictus* for 24 h incubation. The maximum larvicidal activity was observed with the BiONPs against *A. aegypti* (LC_{50}-13.81 and LC_{90}-40.22) and *A. albopictus* (LC_{50}-11.22 and LC_{90}-35.48 ppm) after 24 h of treatment (Table 3). Compared to an aqueous leaf extract, synthesized BiONPs demonstrated excellent larvicidal activity against the two mosquito vectors tested, as shown in Figures 11 and 12. The strong larvicidal activity of synthesized CP-BiONPs can be attributed to their smaller size, which allows them to penetrate the cuticle of insect larvae. The mode of action of such nanoparticles on mosquito vectors has yet to be fully investigated. The toxicity of CP-BiONPs against arthropod vectors may be achieved by the small-size nanomaterials, which allow them to pass past the insect cuticle and into individual cells, as shown in Figure 13. However, in the aquatic environment, more research is required on that exact mode of activity and its antitoxic effects.[48]

6. PHOTOCATALYTIC ACTIVITY

The photocatalytic degradation performance of CP-BiONPs, C-BiONPs, and L-BiONPs against malachite green (MG) and methylene blue (MB) dye has been studied through visible light irradiation approach at a regular time interval of 15 min, and the results are shown in Figure 15.

The characteristic absorption peaks associated with MG and MB occurring at 617 and 664 nm, respectively, are monitored for assessing degradation properties. Before measurements, control experiments are conducted in the absence of a photocatalyst that shows no difference in the initial absorption intensity of dyes. With visible light irradiation, the BiONPs were found to be active in decomposing MG and MB solutions; the rate of degradation differs depending upon the nature of BiONPs used as a photocatalyst. It could be noted that CP-BiONPs outperform the other two BiONPs under study. These findings show that the BiONPs synthesized from CP aqueous leaf extract can promote catalytic dye degradation in the presence of visible light. For efficient photocatalysis, there should be a maximum surface area available for contact between the dye molecule and the photocatalyst. As CP-BiONPs have a smaller particle size, their surface area is more accessible. The mechanical efficiency of a material is determined by the number of active collisions between the

https://doi.org/10.1021/acsomega.3c00792
ACS Omega 2023, 8, 14752−14765

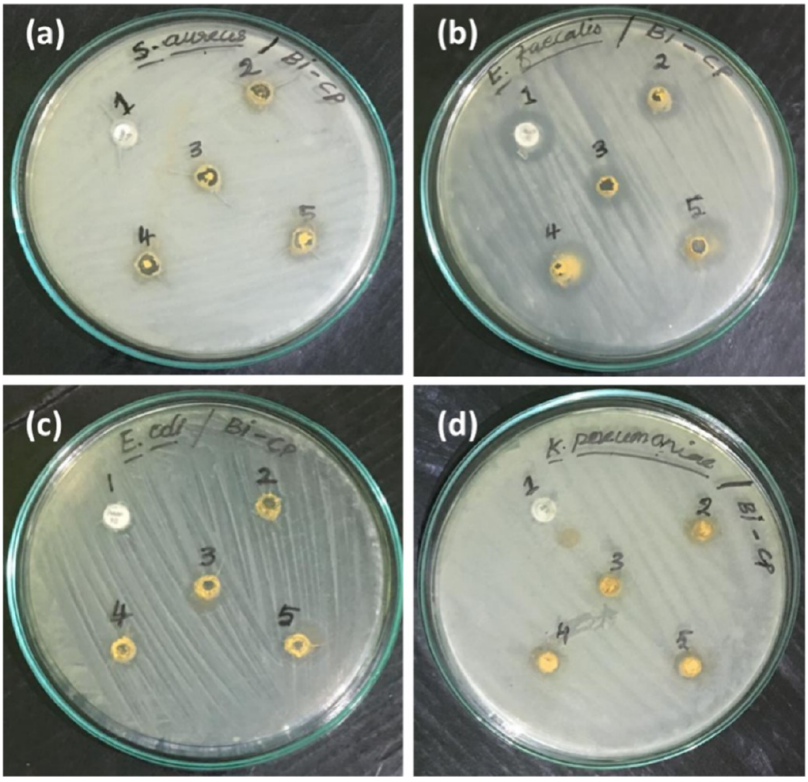

Figure 8. Antibacterial activity of CP-BiONPs with different bacterial pathogens such as *S. aureus* (a), *E. faecalis* (b), *E. coli* (c), and *K. pneumonia* (d).

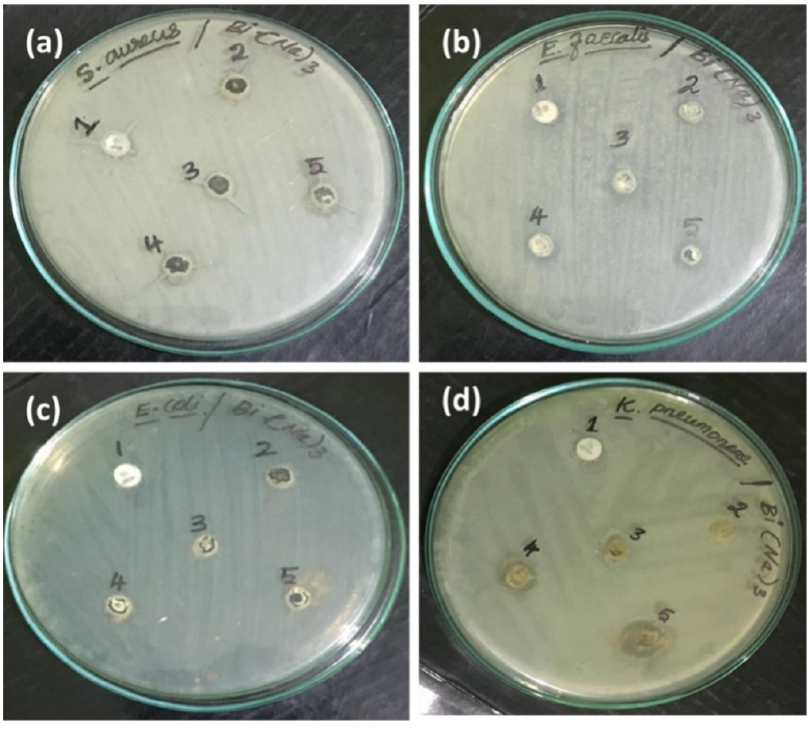

Figure 9. Antibacterial activity of L-BiONPs with different bacterial pathogens such as *S. aureus* (a), *E. faecalis* (b), *E.coli* (c), and *K. pneumonia* (d).

dye molecule and the photocatalyst. Owing to the small particle dimension, CP-BiONPs absorb a higher amount of dye molecules and are involved in a greater number of collisions. As the photocatalytic activity is exceedingly influenced by the rate of adsorption of dye molecules over the surface of the photocatalyst, CP-BiONPs have a greater amount of adsorption, but L-BiONPs and C-BiONPs have a slower rate of degradation. These results pave the way for environmental bioremediation and reveal an effective method for MG and MB dye degradation.[49−53]

https://doi.org/10.1021/acsomega.3c00792
ACS Omega 2023, 8, 14752−14765

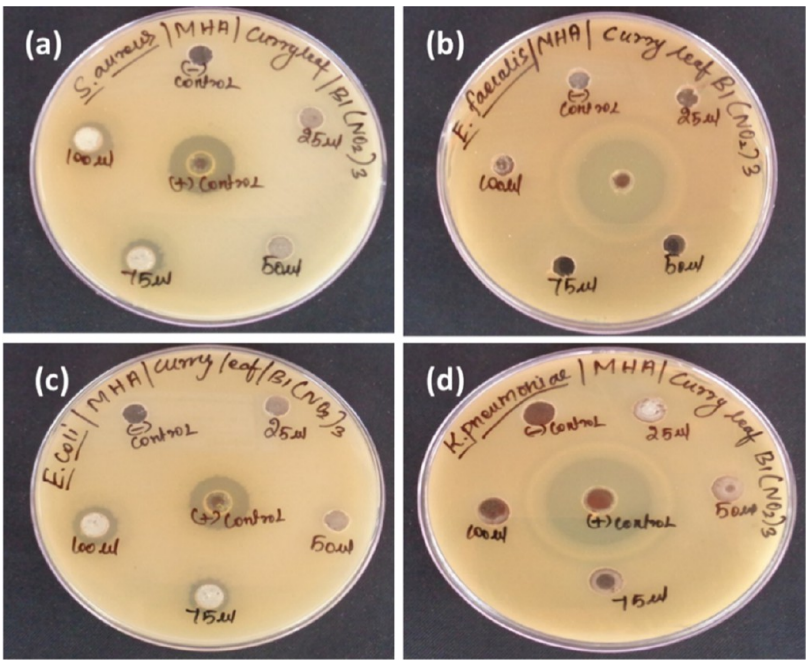

Figure 10. Antibacterial activity of C-BiONPs with different bacterial pathogens such as *S. aureus* (a), *E. faecalis* (b), *E. coli* (c), and *K. pneumonia* (d).

Table 2. Zone of Inhibition of CP-BiONPs, L-BiONPs, and C-BiONPs Activity against *S.aureus*, *E. faecalis*, *E. coli*, and *K. pneumoniae*

	zone of inhibition (mm) CP-BiONPs					zone of inhibition (mm) L-BiONPs					zone of inhibition (mm) C-BiONPs				
name of the pathogens	antibiotic	5 µL	10 µL	15 µL	20 µL	antibiotic	5 µL	10 µL	15 µL	20 µL	antibiotic	5 µL	10 µL	15 µL	20 µL
S. aureus	5.0	0.0	1.0	1.0	1.5	4.0	0.0	0.0	0.0	0.0	5.0	0.0	0.0	0.2	1.0
E. faecalis	6.0	3.0	3.0	5.0	8.0	5.0	0.3	0.3	0.5	3.0	5.0	0.1	0.0	0.0	2.0
E. coli	5.0	0.0	1.0	3.0	5.0	6.0	0.0	0.0	0.5	4.0	8.0	0.0	0.0	0.2	5.0
K. pneumoniae	12.0	0.0	0.0	10.0	10.5	4.0	0.0	0.5	0.0	1.0	4.0	0.0	0.0	0.0	1.0

Table 3. Larvicidal Activity of the Aqueous Extract and the Synthesized BiONPs against *A. aegypti* Larvae and *A.albopictus*

	A. aegypti larvae				*A. albopictus* larvae		
concentration (mg L^{-1})	mortality (%)	LC_{50} (mg L^{-1})	LC_{90} (mg L^{-1})	concentration (mg L^{-1})	mortality (%)	LC_{50} (mg L^{-1})	LC_{90} (mg L^{-1})
25	100.000 ± 0.00	13.81	40.22	25	100.000 ± 0.00	11.22	35.48
20	88.000 ± 4.47			20	88.000 ± 4.47		
15	72.000 ± 8.36			15	72.000 ± 8.36		
10	54.000 ± 5.48			10	54.000 ± 5.48		
5	22.000 ± 8.36			5	22.000 ± 8.36		

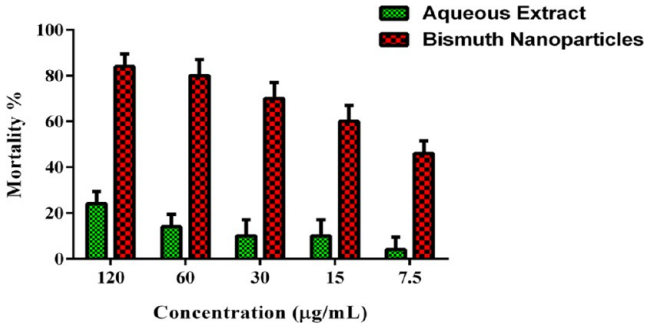

Figure 11. Larvicidal activity of the aqueous extract and the synthesized CP-BiONPs against *A. aegypti*.

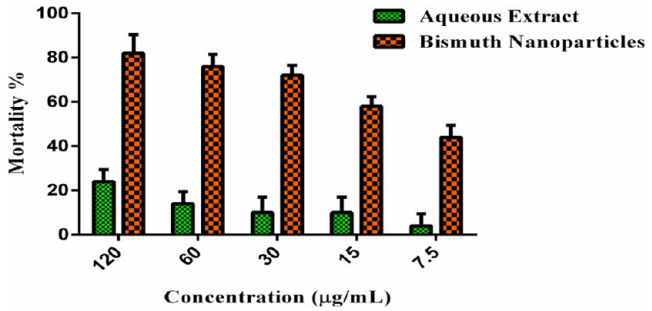

Figure 12. Larvicidal activity of the aqueous extract and the synthesized CP-BiONPs against *A.albopictus*.

Further, a thorough understanding of the mechanism of photocatalytic action is essential for optimizing experimental parameters and identifying an effective photocatalyst for the purification/recycling of industrial effluents. It is well documented in the literature that radical species formed

https://doi.org/10.1021/acsomega.3c00792
ACS Omega 2023, 8, 14752−14765

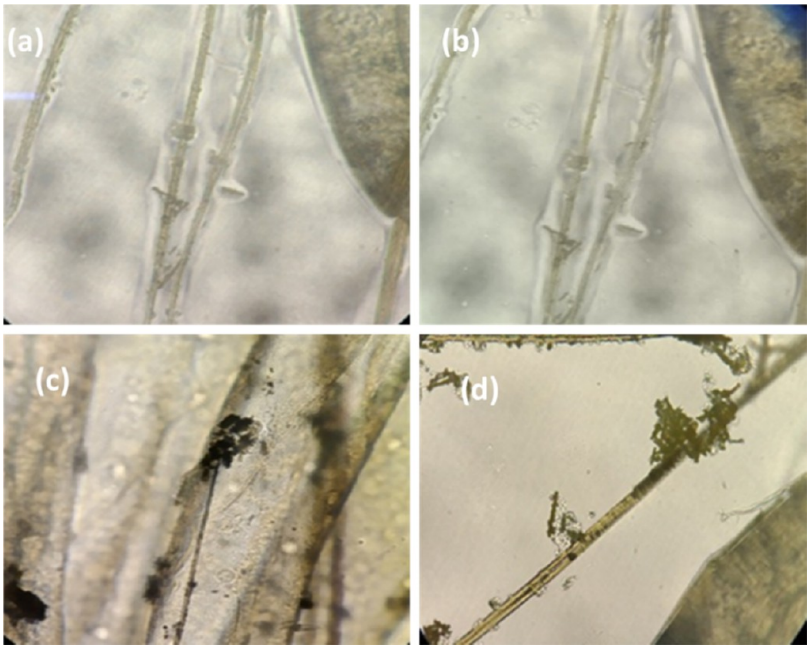

Figure 13. Photographic image of the synthesized BiONPs using the aqueous leaf extract against *A. egyptia* and *A. albopictus* larvae. (a) Control, (b) aqueous leaf extract, and BiONPs (c, d).

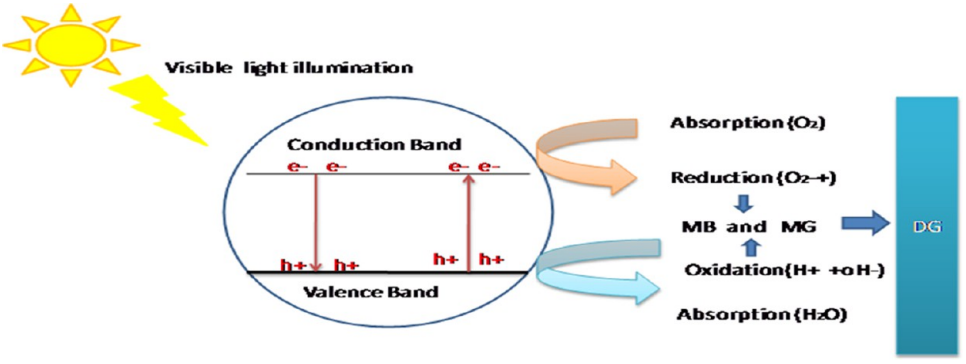

Figure 14. Proposed photocatalytic mechanism.

during the photoexcitation of catalysts actively participate in the degradative dissociation of dye. When visible photons strike nanoparticles in a reaction mixture, the electrons on the particle surface attain an overly excited state and combine with dissolved O_2 molecules to form oxygen anion radicals. As shown in Figure 14, the radicals break down the colorful organic moiety into smaller organic molecules, causing it to degrade rapidly. An ultravisible spectrophotometer with a strong peak at 664 and 617 nm was used to assess the typical absorption of MB and MG. When the irradiation period was increased, the absorption peak intensities gradually decreased. This discovery implies that MB has been successfully photodecolorized.

The image shows the presence of the characteristic BiONP absorption bands (CP−L) (a), (L−L) (b), and (C−L) (c), with absorbance wavelengths of 444 nm (CP−L), 418 nm (C−L), and 404 nm (L−L). The following is an empirical formula

$$(\alpha h\nu)^2 = (h\nu - E_g)$$

It can be used to determine the E_g values (eV) of synthesized nanostructures, where $h\nu$ stands for optical energy and reflects the material's absorptivity coefficient.

The predicted E_g value is derived from the Tauc plot, as shown in Figure 16. The determination that the energy gap associated with L-BiONPs, C-BiONPs, and CP-BiONPs is 4.5, 3.6, and 2.8 eV, respectively, is significant since it indicates that BiONPs are within the UV system's operational range.

The deterioration efficiency (η) was determined using the following formula

$$\eta = \left(1 - \frac{c}{c_0}\right) \times 100$$

where c/c_0 is the time that results in the increase. The degradation performance parameters measured were determined as 70% for MG and 90% for MB. It is to be predicted that the difference in the degradation rate of different dyes arises due to the dissimilar molecular structure and composition. Figure 17 shows the deterioration of MG and MB dye by BiONPs as a function of time, and the apparent rate constant k is determined by linear regression using the following equation: $k = \text{In } c/c_{0/t}$.

The high values of regression coefficients MG (R_2 = 0.70322) and MB (R_2 = 0.93224) in the measured rate fixed values show a favorable linear relationship for the degradation of MG and MB dye by CP-BiONPs. The CP-BiONPs

https://doi.org/10.1021/acsomega.3c00792
ACS Omega 2023, 8, 14752−14765

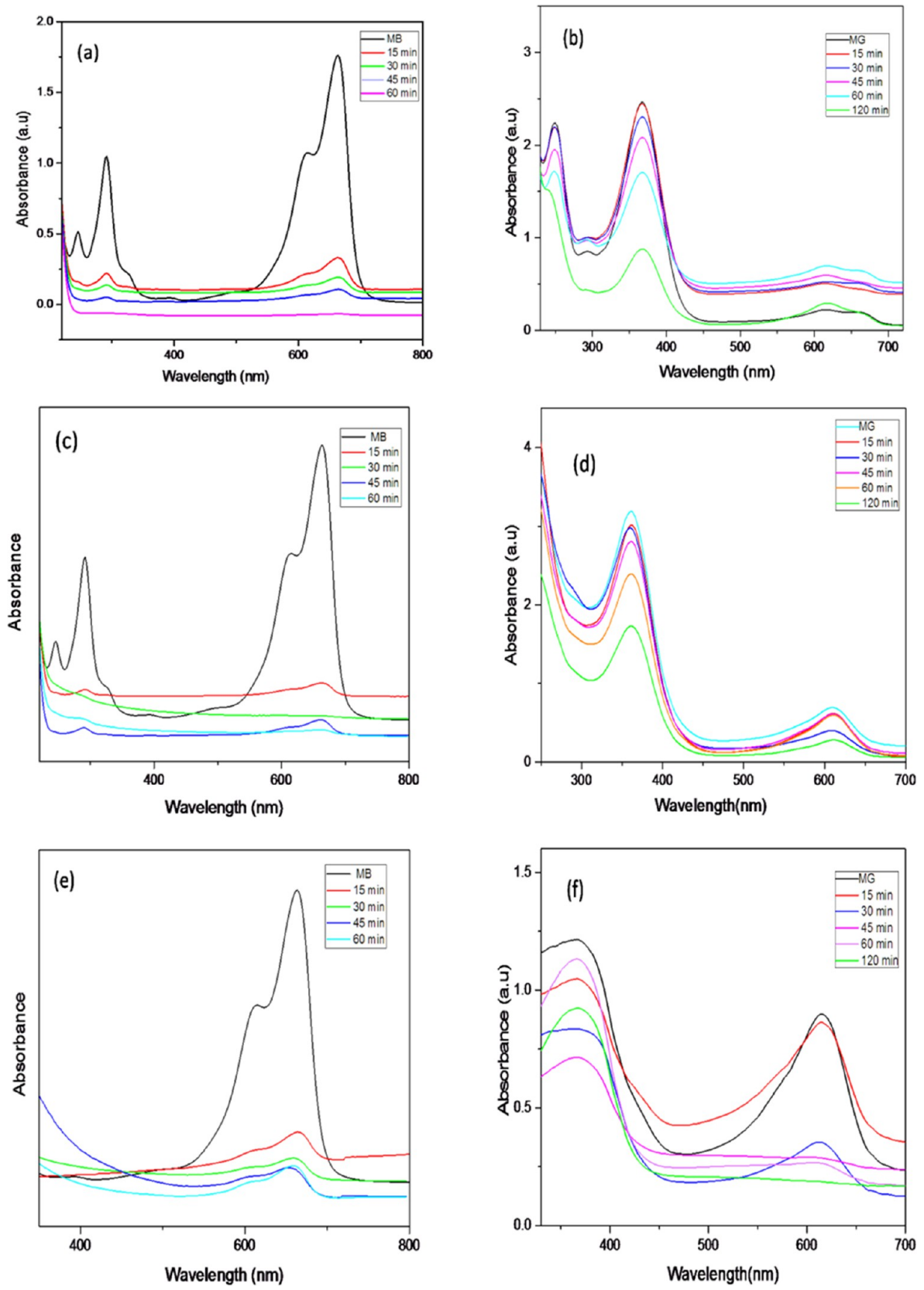

Figure 15. UV−vis absorption of methylene blue: (a) (CP−L), (c) (L−L), and (e) (C−L) and malachite green: (b) (CP−L), (d) (L−L), and (f) (C−L).

exhibited excellent photocatalytic activity against MB degradation with a rate constant of k = 0.00182 min^{-1}. Table 4 shows the antibacterial and photocatalytic activities of diverse bismuth nanostructures. EPR analysis was used to acquire a deeper knowledge and comprehend the mechanism of photocatalysis. As shown in Figure 18, EPR analysis was

https://doi.org/10.1021/acsomega.3c00792
ACS Omega 2023, 8, 14752−14765

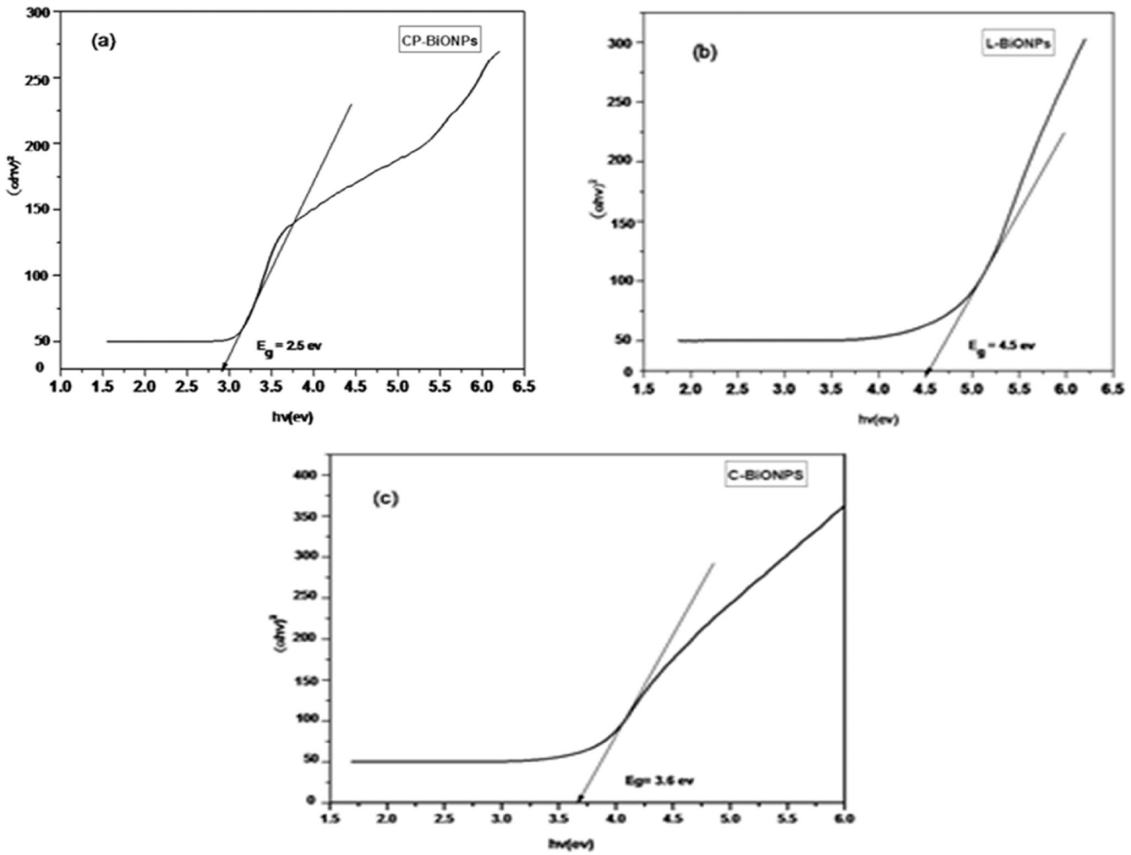

Figure 16. Tauc plot for BiONPS at (CP−L) (a), (L−L) (b), and (C−L) (c).

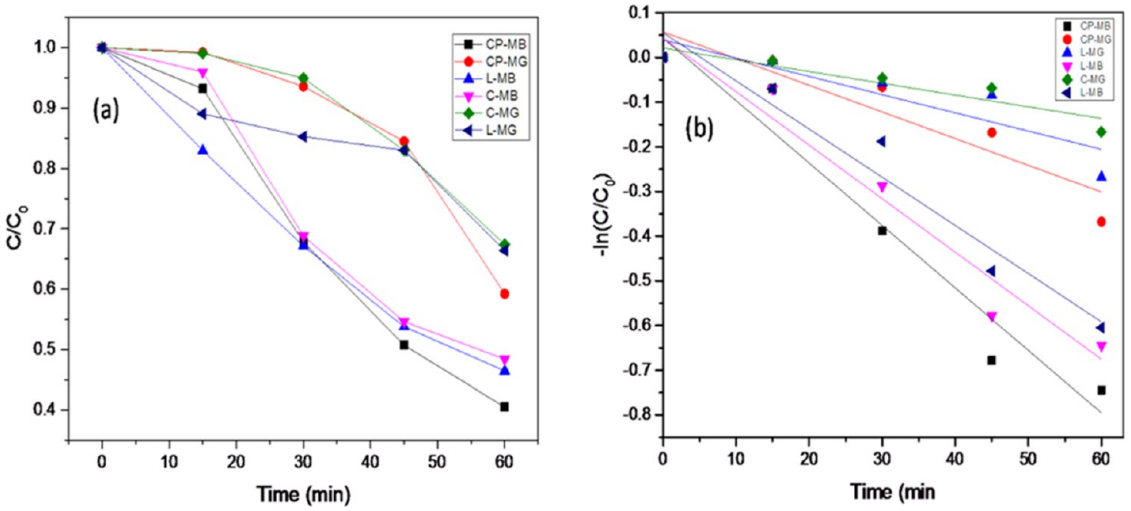

Figure 17. (a) Comparison of the degradation temporal profile of malachite green and methylene blue. (b) Kinetic fit for the degradation.

utilized to evaluate studies on the formation of OH radicals in the in situ illumination process. A glass tube containing CP-BiONPs (0.01 mg), water (50 μL), and DMPO (40 μL) was then exposed to visible light for 25 min while the EPR spectrum was recorded.

The presence of DMPO-OH is confirmed by the peaks at [G] 3411.68, 3426.55, and 3441.32 that match the intensity 1:2:2:1. The g factor, which corresponds to that of a free radical, was found to be between 2.0037 and 2.0056 eV. EPR research has verified the presence of OH radicals in the reaction system when CP-BiONPs are present and exposed to visible light.

7. CONCLUSIONS

In conclusion, this study sheds light on the comparative evaluation of the biological and photocatalytic capabilities of bismuth nanoparticles generated with three distinct leaf extracts. The physicochemical characterization techniques revealed the formation of rod-like crystalline bismuth oxide nanoparticles. An environmentally safe, stable, and effective larvicidal agent against *A. aegypti* and *A. albopictus* larvae, with

https://doi.org/10.1021/acsomega.3c00792
ACS Omega 2023, 8, 14752−14765

Table 4. Data for Comparing Antibacterial and Photocatalytic Activities Pertaining to Diverse Bismuth Nanostructures

s. no		antibacterial activity		photocatalytic activity		
	bismuth nanostructure	against *E. coli*	against *S. aureus*	malachite green	methylene blue	reference
1	mesoporous organosilica supported with bismuth				76.2%	54
2	aqueous solution using bismuth oxyiodide				98.5% in optimum conditions (initial concentration): 10 mg L^{-1}, pH: 9, contact time: 91.25 min	55
3	rhombohedral crystalline bismuth nanoparticles				rate constant 434.7 g^{-1} min^{-1}	56
4	$BiFeO_3$ nanoparticles	9.7 mm for 2% bismuth loading	8 mm for 2% bismuth loading		81% after 120 min	57
5	cobalt and iron codoped bismuth nanoparticles	23 mm	20 mm			58
6	bismuth nanoparticles	18 mm	17.5 mm			59
7	bismuth oxide nanoparticles	2 mm	1 mm			49
8	bismuth ferrite nanorods		1.22 mm			60
9	CP-BiONP	5 mm	1.5 mm	70% for 0.05 g loading	90% 0.05 g loading	present study
10	L-BiONPs	4 mm	nil activity			present study
11	C-BiONPs	5 mm	1 mm			present study

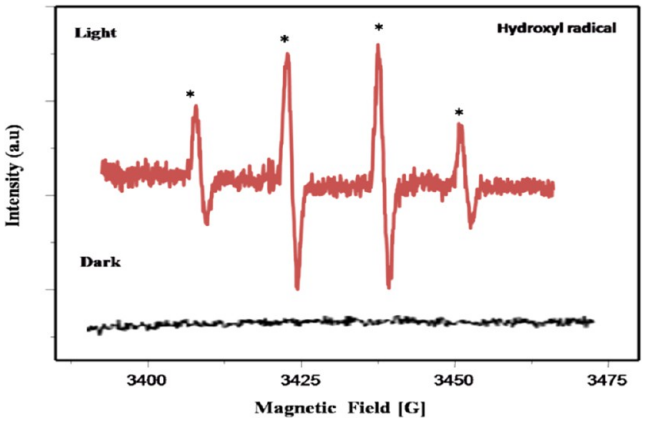

Figure 18. EPR spectrum of CP-BiONPs.

LC_{50} values ranging from 5.53 to 19.24 ppm after 24 h of exposure, was demonstrated to be effective at low concentrations. Under optimal conditions, CP-BiONPs with an E_g value of 2.8 eV showed a maximal photocatalytic degradation efficiency of 90 and 70% against the MB and MG dye, respectively. It provides a positive vision to use the *Coldenia procumbens* leaf extract as a potential phytochemical for synthesizing bismuth oxide nanoparticles with desirable features for water remediation treatment.

AUTHOR INFORMATION

Corresponding Author

Helen P. Kavitha − *Department of Chemistry, Faculty of Engineering and Technology, SRM Institute of Science and Technology, Chennai 600089, Inida;* orcid.org/0000-0002-9099-7937; Email: helenkavithap2020@gmail.com

Author

Prakash Moorthy − *Department of Chemistry, Faculty of Engineering and Technology, SRM Institute of Science and Technology, Chennai 600089, Inida*

Complete contact information is available at: https://pubs.acs.org/10.1021/acsomega.3c00792

Notes

The authors declare no competing financial interest.

ACKNOWLEDGMENTS

The authors are grateful for the support offered by the SRM Institute of Science and Technology, Ramapuram campus, Chennai, India, for permitting research to be conducted there and for providing laboratory space. The SCIF & NRC—SRM Institute of Science and Technology in Kattankulathur helped us in analyzing the samples, for which the authors are very thankful. There are no funds available.

REFERENCES

(1) Nur Hanis, H. H.; Chin, F. S.; Radin, M. S. R. M.; Marlia, M.; Nurfarina, Z.; Nafarizal, N.; Che, Z. Z.; Nor, H. H. A review of nanotechnological applications to detect and control surface water pollution. *Environ. Technol. Innovation* **2021**, *24*, No. 102032.

(2) Nagar, A.; Thalappil, P. Clean Water through Nanotechnology: Needs, Gaps, and Fulfillment. *ACS Nano* **2020**, *14*, 6420−6435.

(3) Liu, Q.; Yiting, L.; Luchao, Y.; Jie, L.; Longcheng, Z.; Tingshuai, L.; Yongsong, L.; Meiling, L.; Jinmao, Y.; Abdulmohsen.; et al. Bi nanoparticles carbon nano sheet composite: A high-efficiency electro catalyst for NO reduction to NH_3. *Nano Res.* **2022**, *15*, 5032−5037.

(4) Lin, Y.; Liang, J.; Li, H.; Zhang, L.; Mou, T.; Li, T.; Yue, L.; Ji, Y.; Liu, Q.; Luo, Y.; et al. Binano dendrites for highly efficient electrocatalytic NO reduction to NH3 at ambient conditions. *Mater. Today Phys.* **2022**, *22*, No. 100611.

(5) Falyouna, O.; Ibrahim, M.; Khaoula, B.; Atsushi, T.; Yuji, S.; Osama, E. Encapsulation of iron nanoparticles with magnesium hydroxide shell for remarkable removal of ciprofloxacin from contaminated water. *J. Colloid Interface Sci.* **2022**, *605*, 813−827.

(6) Joseph, F. O.; Jacinta, F. W.; Thomas, R. G.; Rachel, A. C.; Cara, M. D. Fabrication of a Reusable Carbon Dot/Gold Nanoparticle/Metal−Organic Framework Film for Fluorescence Detection of Lead Ions in Water. *ACS Appl. Mater. Interfaces* **2022**, *14*, 35755−35768.

(7) Chen, K.; Zhang, G.; Li, X.; et al. Electrochemical NO reduction to NH3 on Cu single atom catalyst. *Nano Res.* **2022**, *16*, 5857−5863.

(8) Padmanabhan, P.V.A.; Sreekumar, K. P.; Thiyagarajan, T. K.; Satpute, R. U.; Bhanumurthy, K.; Sengupta, P.; Dey, G. K.; Warrier, K.G.K. Nano-crystalline titanium dioxide formed by reactive plasma synthesis. *Vacuum* **2006**, *80*, 1252−1255.
(9) Gaya, U. I.; Abdullah, A. H. Heterogeneous photocatalytic degradation of organic contaminants over titanium dioxide: a review of fundamentals, progress and problems. *J. Photochem. Photobiol., C* **2008**, *9*, 1−12.
(10) Kumar, A.; Valecha, N.; Jain, T.; Dash, A. P. Burden of malaria in India: retrospective and prospective view. *Am. J. Trop. Med. Hyg.* **2007**, *77*, 69−78.
(11) Rao, T. R.Malaria Research Unit(ICMR), Delhi. The Anophelines of India, 1984, p 518.
(12) Dhanda, V.; Kaul, H. N. Mosquito vectors of Japanese encephalitis virus and their bionomics in India. *Proc. Indian Natl. Sci. Acad.* **1980**, *46*, 759−768.
(13) Liu, N.; Xu, Q.; Zhu, F.; Zhang, L. Pyrethroid resistance in mosquitoes. *Insect Sci.* **2006**, *13*, 159−166.
(14) Lee, S. E.; Kim, J.; Lee, S. Insecticide resistance in increasing Interest. *Agric. Chem. Biotechnol.* **2001**, *44*, 105−112.
(15) Casida, J. E.; Quistad, G. B. Insecticide targets: learning to keep up with resistance and changing concepts of safety. *Agric Chem. Biotechn ol.* **2000**, *43*, 185−191.
(16) Yang, Y. C.; Lee, S. G.; Lee, H. K.; Kim, M. K.; Lee, S. H.; Lee, H. S. piperidine amide extracted from *Piper longum* L. fruit shows activity against *Aedes aegypti* mosquito larvae. *J. Agric. Food Chem.* **2002**, *50*, 3765−3767.
(17) Rahuman, A. A.; Venkatesan, P. Larvicidal efficacy of five cucurbitaceous plant leaf extracts against mosquito species. *Parasitol. Res.* **2008**, *103*, 133−139.
(18) Amer, A.; Mehlhorn, H. Repellency effect of 41 essential oils against Aedes, Anopheles, and Culex mosquitoes. *Parasitol. Res.* **2006**, *99*, 478−490.
(19) Rahuman, A. A.; Bagavan, A.; Kamaraj, C.; Vadivelu, M.; Zahir, A. A.; Elango, G.; Pandiyan, G. Evaluation of indigenous plant extracts against larvae of *Culex quinquefasciatus* Say (Diptera: Culicidae). *Parasitol. Res.* **2009**, *104*, 637−643.
(20) Bhattacharya, D.; Gupta, R. K. Nanotechnology and potential of microorganisms. *Crit. Rev. Biotechnol.* **2005**, *25*, 199−204.
(21) Sinha, S.; Pan, I.; Chanda, P.; Sen, S. K. Nanoparticles fabrication using ambient biological resources. *J. Appl. Biosci.* **2009**, *19*, 1113−1130.
(22) Morones, J. R.; Elechiguerra, J. L.; Camacho, A.; Holt, K.; Kouri, J. B.; Ramfrez, J. T.; Yacaman, M. J. The bactericidal effect of silver nanoparticles. *Nanotechnology* **2005**, *16*, 2346−2353.
(23) Iravani, S. Green synthesis of metal nanoparticles using plants. *Green Chem.* **2011**, *13*, 2638−2650.
(24) Tavakoli, F.; Salavati-Niasari, M.; Niasari, M. S.; badiei, A.; Mohandes, F. Green synthesis and characterization of graphene nanosheets. *Mater. Res. Bull.* **2015**, *63*, 51−57.
(25) Negar, M. K.; Masoumeh, Y. Green Synthesis and Characterization of Bismuth Oxide Nanoparticle Using Mentha Pulegium Extract. *Iran. J. Pharm. Res.* **2020**, *19*, 70−79.
(26) Venkat, S. K.; Shanmugam, S. Photocatalytic and antibacterial activity of bismuth and copper codoped cobalt ferrite nanoparticles. *J. Mater. Sci.: Mater. Electron.* **2018**, *29*, 8738−8746.
(27) Zeeshan, H. J.; Ather, A.; Sze-Mun, L.; Sanghun, P.; Kangmin, C.; Eun-Sik, K.; Kyung, H. C. Machine learning approaches to predict the photocatalytic performance of bismuth ferrite-based materials in the removal of malachite green. *J. Hazard. Mater.* **2023**, *442*, No. 130031.
(28) Zi, J. Y.; Sze, M. L.; Jin, C. S.; Honghu, Z.; Abdul, R. M.; Zeeshan, H. J. Boosting sunlight-powered photocatalytic fuel cell with S-scheme Bi_2WO_6/ZnO nanorod array composite photoanode. *Inorg. Chem. Commun.* **2022**, *143*, No. 109826.
(29) Jin, C. S.; Sze, M. L.; Honghu, Z.; Hua, L.; Haixiang, L.; Liangliang, H.; Kai, O. T.; Abdul, R. M.; Jun, W. L. Enhanced synchronous photocatalytic 4-chlorophenol degradation and Cr(VI) reduction by novel magnetic separable visible-light-driven Z-scheme $CoFe_2O_4$/P-doped BiOBr heterojunction nanocomposites. *Environ. Res.* **2022**, *212*, No. 113394.
(30) Fan, H. T.; Pan, S. S.; Teng, X. M.; Ye, C.; G H Li, L. D.; Zhang. *δ*-Bi2O3 thin films prepared by reactive sputtering: Fabrication and characterization. *Thin Solid Films* **2006**, *513*, 142−147.
(31) Zeeshan, H. J.; Abbas, A.; Sze, M. L.; Sanghun, P.; Kangmin, C.; Eun, S. K.; Kyung, H. C. Machine learning approaches to predict the photocatalytic performance of bismuth ferrite-based materials in the removal of malachite green. *J. Hazard. Mater.* **2023**, *442*, No. 130031.
(32) Zi, J. Y.; Sze, M. L.; Jin, C. S.; Honghu, Z.; Abdul, R. M.; Zeeshan, H. J. Boosting sunlight-powered photocatalytic fuel cell with S-scheme Bi2WO6/ZnO nanorod array composite photoanode. *Inorg. Chem. Commun.* **2022**, *143*, No. 109826.
(33) Sin, J. C.; Lam, S. M.; Zeng, H.; Lin, H.; Li, H.; Huang, L.; Tham, K. O.; Mohamed, A. R.; Lim, J. W. Enhanced synchronous photocatalytic 4-chlorophenol degradation and Cr(VI) reduction by novel magnetic separable visible-light-driven Z-scheme $CoFe_2O_4$/P-doped BiOBr heterojunction nanocomposites. *Environ. Res.* **2022**, *212*, No. 113394.
(34) Shui, W. C. C.; Ding, Q. N.; Dileep, K.; Sze, M. L.; Zeeshan, H. J. Investigating the effects of various synthesis routes on morphological, optical, photoelectrochemical and photocatalytic properties of single-phase perovskite BiFeO3. *J. Phys. Chem. Solids* **2022**, *160*, No. 110342.
(35) Jin, C. S.; Sze, M. L.; Honghu, Z.; Hua, L.; Haixiang, L.; Kai, O. T.; Abdul, R. M.; Jun, W. L.; Zuzeng, Q. Magnetic NiFe2O4 nanoparticles decorated on N-doped BiOBr nanosheets for expeditious visible light photocatalytic phenol degradation and hexavalent chromium reduction via a Z-scheme heterojunction mechanism. *Appl. Surf. Sci.* **2021**, *559*, No. 149966.
(36) Patil, C. D.; Patil, S. V.; Borase, H. P.; Salunke, B. K.; Salunkhe, R. B. Larvicidal activity of silver nanoparticles synthesized using Plumeria rubra plant latex against Aedes aegypti and Anopheles stephensi. *Parasitol. Res.* **2012**, *110*, 1815−1822.
(37) Sierra-Fernandez, A.; De la Rosa-García, S. C.; Gomez-Villalba, L. S.; et al. Synthesis, Photocatalytic, and Antifungal Properties of MgO, ZnO and Zn/Mg Oxide Nanoparticles for the Protection of Calcareous Stone Heritage. *ACS Appl. Mater. Interfaces* **2017**, *9*, 24873−24886.
(38) Krishnamoorthy, K.; Moon, J. Y.; Hyun, H. B.; et al. Mechanistic Investigation on the Toxicity of MgO Nanoparticles toward Cancer Cells. *J. Mater. Chem.* **2012**, *22*, 24610−24617.
(39) Naeimi, H.; Alishahi, N. J. Nanocrystalline magnesium oxide as solid base catalyst in the presence of iodine promoted one-pot synthesis of 2-substituted benzimidazole derivatives under mild conditions. *Exp. Nanosci.* **2015**, *10*, 222−234.
(40) Finney, D. J. *Probit Analysis*; Cambridge University Press: Cambridge, 1971; Vol. 3, p 32.
(41) Johan, S.; Kezia, I.; Christina, A.; Kartini, K.; Esrat, R.; Deok, C. Y. Scale-up of green synthesis and characterization of silver nanoparticles using ethanol extract of *Plantago major* L. leaf and its antibacterial potential. *S. Afr. J. Chem. Eng.* **2021**, *38*, 1−8.
(42) Thangavel, S.; Sambandam, A.; Luis, G.; Detlef, W. B.; Muthupandian, A. Phase-controlled synthesis of bismuth oxide polymorphs for photocatalytic applications. *Mater. Chem. Front.* **2018**, *2*, 1664−1673.
(43) Amin, J. A.; Laouini, S. E.; Bouafia, A.; Alonso, M. G.; Guerrero, A.; Romero, A. Green synthesis and characterization of iron oxide nanoparticles by phoenix dactyl lifera leaf extract and evaluation of their antioxidant activity. *Sustainable Chem. Pharm.* **2020**, *17*, 2352−5541.
(44) Drishya, S.; Namitha, R.; Smera, P. J.; Vimala, J.; Paulson, M. Synthesis of silver and copper oxide nanoparticles using *Myristicafragrans* fruit extract Antimicrobial and catalytic applications. *Sustainable Chem. Pharm.* **2020**, *16*, 2352−5541.
(45) Bindhani, B. K.; Panigrahi, A. K. Biosynthesis and Characterization of Silver Nanoparticles (SNPs) by using Leaf Extracts of

https://doi.org/10.1021/acsomega.3c00792
ACS Omega 2023, 8, 14752−14765

Ocimum Sanctum L (Tulsi) and Study of its Antibacterial Activities. *J. Nanomed. Nanotechnol.* **2015**, *S6*, 2157−7439.
(46) Athiralakshmy, T. R.; Divyamol, A. S.; Nisha, P. Phytochemical screening of Saracaasoca and antimicrobial activity against bacterial species. *Asian J. Plant Sci. Res.* **2016**, *6*, 30−36.
(47) Bhuyan, T.; Mishra, K.; Prasad, R.; et al. Biosynthesis of zinc oxide nanoparticles from Azadirachtaindica for antibacterial and photocatalytic applications. *Mater. Sci. Semicond. Process.* **2015**, *32*, 55−61.
(48) Giovanni, B.; Filippo, M.; Donato, R.; Cesare, S.; Baskaralingam, V.; Suresh, K.; H Akon, H.; Abdullah, A. A.; Heinz, M.; Angelo, C. Nanoparticles as effective acaricides against ticks—a Review. *Ticks Tick-Borne Dis.* **2017**, *8*, 821−826.
(49) Motakef, K. N.; Yaqoubi, M. Green Synthesis and Characterization of Bismuth Oxide Nanoparticle Using Mentha Pulegium Extract. *Iran. J. Pharm. Res.* **2020**, *19*, 70−79.
(50) Prakash, M.; Helen, P. K.; S Abinaya, S.; Jasmine, P. V.; Lohita, D. Green synthesis of bismuth based nanoparticles and its applications - A review. *Sustainable Chem. Pharm.* **2022**, *25*, 2352−5541.
(51) Negar, M. K.; Atefeh, A. Methylene blue adsorption from aqueous solution using Zn2 (BDC) 2 (DABCO) metal organic framework and its polyurethane nanocomposite. *Iran. J. Chem. Chem. Eng.* **2022**, *41*, No. 12.
(52) Motakef, K.; Negar, M. R.; Sima, T. D.; Masoumeh, Y. Synthesis and characterization of bismuth oxide nanoparticle by thermal decomposition of bismuth-based MOF and evaluation of its nanocomposite. *J. Environ. Chem. Eng.* **2021**, *40*, 11−19.
(53) Ghourchian, F.; Motakef-Kazemi, N.; Ghasemi, E.; Ziyadi, H. Zn-based MOF-chitosan-Fe3O4 nanocomposite as an effective nanocatalyst for azo dye degradation. *Environ. Chem. Eng.* **2021**, *9*, No. 106388.
(54) Shahzad, K.; Fernandez, G. J.; Khan, M. I.; Shanableh, A.; Khan, N. A.; Rehman, A. Formulation of Bismuth (Bi2O3) and Cerium Oxides (CeO2) Nanosheets for Boosted Visible Light Degradation of Methyl Orange and Methylene Blue Dyes in Water. *Catalysts* **2022**, *12*, No. 1197.
(55) Sedigheh, M.; Mojtaba, A.; Mahmoud, T.; Najmeh, A. K.; Aliakbar, D. Photocatalytic degradation of methylene blue dye using bismuth ox iodide from aqueous solutions. *Int. J. Environ. Anal. Chem.,* **2022**, *10*, 1−13.
(56) Mahiuddin, M. D.; Bungo, O. Comprehensive Study on Lemon Juice-Based Green Synthesis and Catalytic Activity of Bismuth Nanoparticles. *ACS Omega* **2022**, *7*, 35626−35634.
(57) Sharmila, M.; Jothi, M. R.; Parvathiraja, C.; Abdul Kader, S. M.; Siddiqui, M. R.; Wabaidur, S. M.; Islam, M. A.; Lai, W.-C. Visible Light Photocatalyst and Antibacterial Activity of BFO (Bismuth Ferrite) Nanoparticles from Honey. *Water* **2022**, *14*, No. 1545.
(58) Kirankumar, V. S.; Sumathi, S. Photocatalytic and antibacterial activity of bismuth and copper co-doped cobalt ferrite nanoparticles. *J. Mater. Sci: Mater. Electron.* **2018**, *29*, 8738−8746.
(59) Sally, S. H.; Raad, M. S. A.; Kadhim, A. H. Temperature Effects on the Optical Properties of Bismuth Nanoparticles prepared by PLAL for Antibacterial Activity. *Int. J. Nanoelectron. Mater* **2022**, 1−12.
(60) Kunal, B.; Debashis, D.; Jaya, B.; Nabanita, D.; Subhasis, R.; Pintu, S.; Sujit, K. B.; Chakraborty, P. K. Enhanced polarization, magnetic response and pronounced antibacterial activity of bismuth ferrite nanorods. *Mater. Chem. Phys.* **2017**, *195*, 207−213.

https://doi.org/10.1021/acsomega.3c00792
ACS Omega 2023, 8, 14752−14765